In-Situ Generation of CO_x-Free H_2 by Catalytic Ammonia Decomposition over Ru-Al-Monoliths.

Sabino Armenise[a,b,c *], Fernando Cazaña[b], Antonio Monzón[b], Enrique García-Bordejé[c]

[a] Universidad Politécnica Salesiana, Department of Biotechnology, Av. 12 Octubre, 170109, Quito, Ecuador.

[b] Institute of Nanoscience of Aragon. Department of Chemical and Environmental Engineering. University of Zaragoza. 50018, Zaragoza. Spain

[c] Instituto de Carboquímica (ICB-CSIC), Miguel Luesma Castán 4, 50018 Zaragoza, Spain.

Abstract

Ru catalysts supported on alumina coated monoliths has been prepared employing three different precursor, which are ruthenium chloride, ruthenium nitrosyl nitrate and ruthenium acetyl acetonate, by an equilibrium adsorption method. The Ru particle sizes could be controlled varying the metal precursor salt. Among the prepared catalysts, Ru catalyst prepared from nytrosyl nitrate exhibited the highest activity which is concomitant to the largest mean Ru particle size of 3.5 nm. The values of the apparent activation energy calculated from the Arrhenius equation are according to the Temkin-Phyzev model, indicating that the recombinative desorption of N ad-atoms is the rate-determining step of the reaction. However, the ratio between the kinetic orders with respect to ammonia and hydrogen (-α/β), is not in agreement to the valued predict by Temkin formalism. This fact could be related to the different operational conditions used during the reaction, and/or catalyst nature, but not to any change on the controlling step of the reaction.

Keywords: Structured Reactors; Ru-Catalyst; Ammonia Decomposition; Kinetics; COx-Free; Nanoparticle.

* Corresponding author. Tel.:+ 593 994787533; Email: sarmenise@ups.edu.ec

1. Introduction

Hydrogen combined with PEM fuel cells have attracted great interest recently as substitute of fossil fuels in locomotion and other fields. However, hydrogen storage and transportation involves great technical challenges to overcome. Its low energy per volume unit, along with its flammability are factors which make difficult its storage as gas at normal pressure [1]. Because of that, several technologies for hydrogen storage have been proposed. These include storage at high pressures, either in liquid form or adsorbed in a solid [2,3]. However, liquid H_2 requires high energy consumption and expensive leak-free tanks. A more interesting option is the chemical storage in form of easily storable and with high hydrogen content compounds, such as light hydrocarbons or ammonia. These compounds must be decomposed in-situ to release a hydrogen stream to feed the fuel cell. Recently, the production of hydrogen from the decomposition of light hydrocarbons as methane, ethane or ethanol has attracted a great researching interest [4]. Nevertheless, all these processes have the inherent drawback of producing CO_x along with the H_2 stream. CO_x acts as poisons for PEM fuel cells, even at concentrations as low as a few ppm [5]. Therefore, systems based on hydrocarbons decomposition must include a series of purification steps, like desulfurization, water gas shift, methanation, and preferential oxidation to reduce CO_x levels in the reformer outlet gas. Ammonia, on the other hand, produces a CO_x-free stream of hydrogen, and unconverted ammonia can be easily reduced to safe levels in one-step adsorption. In addition, ammonia has a high H_2 content (17.7% wt) and can be stored in liquid form at mild conditions (room temperature and 6 atms). For the whole process of H_2 storage as NH_3 to be environmentally sustainable, the H_2 and the energy required for synthesis and decomposition process should be produced using renewable energies. On the other

hand, the energy needed for decomposition of NH_3 could be generated using a small percentage of the energy stored in NH_3. This percentage will be minimized if a catalyst active at the lowest temperature as possible is used and obtaining a high-purity H_2 stream. All this characteristic make more economically feasible the hydrogen production from ammonia than others career [6].

In the last years, ammonia decomposition reaction has been extensively studied for H_2 generation, including the catalytic active phase to the reactor structure and design [7]. Yin et al., reported that ruthenium exhibits the highest TOF in ammonia decomposition [8]. Therefore, research has been focused on ruthenium supported on different carriers, such as alumina [9–11] or others transition metal oxides like MgO [12], activated carbon [13,14], or carbon nanotubes/nanofibers [15–18]. Bimetallic combinations of transition metals (MoCo) have also proved to be active enough to replace ruthenium catalyst [19–23]. From the point of view of reactor design, microestructured reactors have improved the performance of the conventional packed bed reactors [24–27].

One century after the development of Habber-Bosch process, ammonia mechanism still being investigated by several authors to obtain more precise information about reaction mechanism and to explain the wide range differences observed on the kinetic parameters.

The mechanism of ammonia decomposition reaction has been grouped in two limiting cases: (i) effect of ammonia concentration, (ii) effect of hydrogen concentration.

At low ammonia concentrations and low temperatures [28,29], the reaction rate shows non-dependence with respect to ammonia. However, at high temperatures the reaction becomes first-order with respect to ammonia [30,31]. These transition temperature has been investigated by Tamaru [32] and Chellappa [33], and explained by a change of reaction mechanism. At temperature below 650 K the recombinative desorption of N-

adsorbed species is the rate-determining step (RDS), while at high temperature (< 750 K), cleavage of N-H bond on NH_3 adsorbed species is the RDS [30,31].

At high hydrogen partial pressure and low temperature, the reaction is found to be inhibited by hydrogen [33]. In these operational conditions the reaction is explained by Temkin-Phyzev mechanism [32,34]. This reaction mechanism assumes that both recombinative desorption of N-species and N-H cleavage are the RDS. Inhibitory effects of hydrogen could be associated to the re-hydrogenation of N-species adsorbed or by blocking the active sites by competitive adsorption, where ammonia decomposition takes place. At high temperature and low hydrogen partial pressure (low conversion), Temkin-Phyzev model could be re-written as Tamaru`s model [32,35].

This work is a new contribution of our group to the study of the ammonia decomposition reaction, using nickel catalysts supported on honeycomb monoliths prepared by electrostatic adsorption structured reactors [27]. Herein, our aim is to investigate the performance of Ru-based reactors, and , to obtain uniformly dispersed Ru nanoparticles in alumina coated monoliths. To this end, different Ru precursors were tested. The catalysts after reduction were characterized by STEM, TPR and XPS and tested in the decomposition of pure ammonia. Also, a kinetic study is carried out in other to determine the effect of precursor synthesis on the main apparent kinetic parameters: activation energy and reaction orders.

2. Experimental

2.1. Materials and Catalyst Preparation

Cordierite monoliths were carved out from blocks supplied by Corning (400 cpsi) to the desired dimensions (65 mm long, 10 mm diameter, ca. 2,4 g). These monoliths were impregnated with alumina by a dip coating method, as described elsewhere [27]. A sol-gel was prepared by mixing pseudobohemite (AlOOH pural, from Sasol), 0.3 M nitric

acid and urea, in 2:5:1 proportion. After stirring for 24h, monoliths were immersed in the mixture until ensuring the absence of air bubbles in the channels. Following up, the excess of liquid was removed with pressurized air and the monoliths were dried for 24 hours at room temperature while rotating around its axis. Later, the monoliths were thermally treatment under 100 ml/min air flow for 2 hours at 873 K, at a heating rate of 1 K/min.

The deposition of ruthenium nanoparticles was carried out by equilibrium adsorption or electrostatic adsorption method [36]. In this method, the ions of precursor in solution are bound by electrostatic forces to the sites of opposite charge at support surface. Three different Ru precursors were used. Ruthenium Chloride ($RuCl_3 \cdot xH_2O$) dissolved in 10 ml of 0.1M HCl, ruthenium nitrosyl nitrate ($Ru(NO_3)_3(NO)$) dissolved in 10 ml of distilled water and ruthenium acetyl acetonate ($RuC_{15}H_{21}O_6$) dissolved in 10 ml of toluene. The weight or ruthenium in solution was calculated on the basis of a nominal weight percentage of 5 wt% with respect to alumina coating. The alumina coated monoliths were fitted to a vial with the impregnating solution and rotated continuously perpendicular to its axis for 24 hours. In this process, the liquid with the precursor flows through the monoliths channels and it is concomitantly homogenized due to the rotating movement. After this process, the liquid inside the channels was removed with pressurized air and the monoliths were dried under rotation for 24 hours. Finally, they were calcined in 100 ml/min of N_2 at 873 K during 2 h, using a heating rate of 1 K/min. The monolith samples were denoted as Ru(Cl)/Al/M, Ru(NN)/Al/M and Ru(acac)/Al/M for catalysts prepared from ruthenium chloride, ruthenium nitrosyl nitrate and ruthenium acetyl acetonate, respectively.

Deposition of metal by electrostatic adsorption or ion-exchange it is useful way to incorporate well-dispersed metal in different kinds of supports. This technique should

get a balance in the equilibrium between the charges on the surface of support, and the charge of metal-ions in solution. For this reason, achieving a desired metal-loading it is not a trivial problem, and it is necessary make successive impregnations by this technique.

However, for supports like pellets, or other configurations where the layer thickness or particle radius are bigger than few microns, metal-ions diffusion into the particle or support may be difficult. For conventional catalyst supports, this will result in egg-shell-type metal distributions. This kind of problems can be avoided choosing specific complex-metal, which can lead to slow adsorption process [37].

During the first step of this work (no presented here), we analyze the effects of successive metal deposition (specifically nickel metal) and enhanced the metal adsorption by process in a vacuum system, to increase the weight/volume ratios. The results obtained shows both process increase the metal loading, but with any positive effect on the catalytic ammonia decomposition reaction may be related to lower dispersion reached by the impregnation process.

The actual Ru content was analyzed by inductive coupled plasma optical emission spectroscopy (ICP-OES) after digestion of the samples in lithium borohydride. In addition, Ni catalyst was also prepared from a nickel nitrate solution as described previously [23]. The actual Ni loading determined by ICP-OES was 15 wt%.

It is well-knew that the stability of the catalytic coating is closely related to adhesion strength of alumina-washcoated on the monolith walls, and is a key step to be evaluated to scale up this kind of catalyst to real use. The stability of the catalytic coatings were measured by ultrasonication for 30 min and reported in previous work by our group [38]. These results indicate that catalytic coating is properly attached to the walls. Despite that case we had nanofibers deposited on alumina washcoated on monolith

reactor, the washcoated alumina was produced in the same way those presented in this work, and then the result can be extrapolated.

2.2. Catalytic Testing

Catalyst reactivity system consists of a continuous-flow 15 mm i.d. quartz reactor inside horizontal furnace with a temperature controller (Eurotherm). The monolithic nickel catalyst was wrapped with quartz stripe and it was tightly fitted to the wall of the quartz reactor to avoid channeling. Subsequently, the reactor was placed in the constant temperature zone of the furnace. The reaction testing was carried out after catalyst reduction in hydrogen atmosphere (100 ml/min H_2:N_2, 50:50) at 773 K for 1 h. Catalysts were tested between 573 and 973 K using 100 ml/min of pure anhydrous ammonia as feed gas. The outlet reaction gases were analyzed with an Agilent Micro GC 3000A. H_2 an N_2 were analyzed in a molsieve column and ammonia in a Plot-Q column. To ensure repeatability, 2–3 separate GC samples were taken and averaged for each experimental data point, and analyses were typically within ±3% of each other. The conversion was calculated taking into account the variations in the flow due to the mole increase in the reaction.

2.3. Catalyst Characterization

The catalysts after reaction were tested by different techniques. Temperature programme reduction (TPR) was carried out in a Micromeritics AutoChem II 2920. In TPR experiments, the catalyst was heated in 50 ml/min (STP) of 10% H_2 in Ar up to 1273 K with a heating rate of 10 K/min.

XPS technique was used to measure the Ru oxidation state. The apparatus was an ESCAPlus Omnicrom system equipped with a Mg Kα radiation source to excite the

sample. Calibration of the instrument was done with Ag $3d_{5/2}$ line at 368.27eV. All measurements were performed under UHV, better than 10^{-10} Torr. Internal referencing of spectrometer energies was made using the dominating Al 2p peak of the support, at 74.0 eV and corroborated with the C 1s signal at 284.4 eV. The curve fitting of the spectra was performed using CASA XPS software after applying a Shirley baseline.

Catalyst particle size was studied by scanning transmission electron microscopy (STEM) using a FEI TECNAI F30 electron microscope equipped with Gatan Energy Filter and cold field emission gun (FEG) operated at 300 kV with 1.5 Å lattice resolution. TEM specimens were prepared by ultrasonic dispersion in ethanol of powder retrieved from the monoliths. A drop of the suspension was applied to a holey carbon support grid.

3. Results and Discussion

3.1 Textural and morphological characterization

Table 1 shows the textural properties of the prepared catalysts. All Ru catalysts exhibit similar textural properties and the surface area is comparable to that of the support (246 m^2/g). There are not significant differences between the Ru content deposited using the different salt precursors.

Table 1. Textural properties measured by N_2 physisorption and surface composition measured by XPS of Ru catalysts on alumina coated monoliths prepared from different precursors.

Catalyst	Ru/Al [1] wt. %	Surface Area (m^2/g)	Pore diameter (nm)	Ru/Al[2] wt. %	Ru^0/Ru_{total}[2] at. %
Ru(NN)/Al/M	3.0	238	6.0	6.7	69.1
Ru(Cl)/Al/M	3.6	215	6.0	6.4	5.7
Ru(acac)/Al/M	3.0	233	5.5	5.6	7.4

[1] Measured by ICP-OES
[2] Measured by XPS

The ruthenium particle size was characterized by STEM. Fig. 1 shows representative STEM images and particle size distribution (inset) for the several catalysts prepared. For Ru(NN)/Al/M (Fig. 1a, and 1b) the particles are spherical with heterogeneous distribution particle sizes, ranging between 1 and 10 nm with a mean size of 3.5 nm. On the other hand, for Ru(Cl)/Al/M and Ru(acac)/Al/M (Fig. 1c to 1f) the particle size are predominantly smaller than 1.5 nm, with a homogeneous distribution. The mean particle size is subnanometric for Ru(Cl)/Al/M and 1.5 nm for Ru(acac)/Al/M.

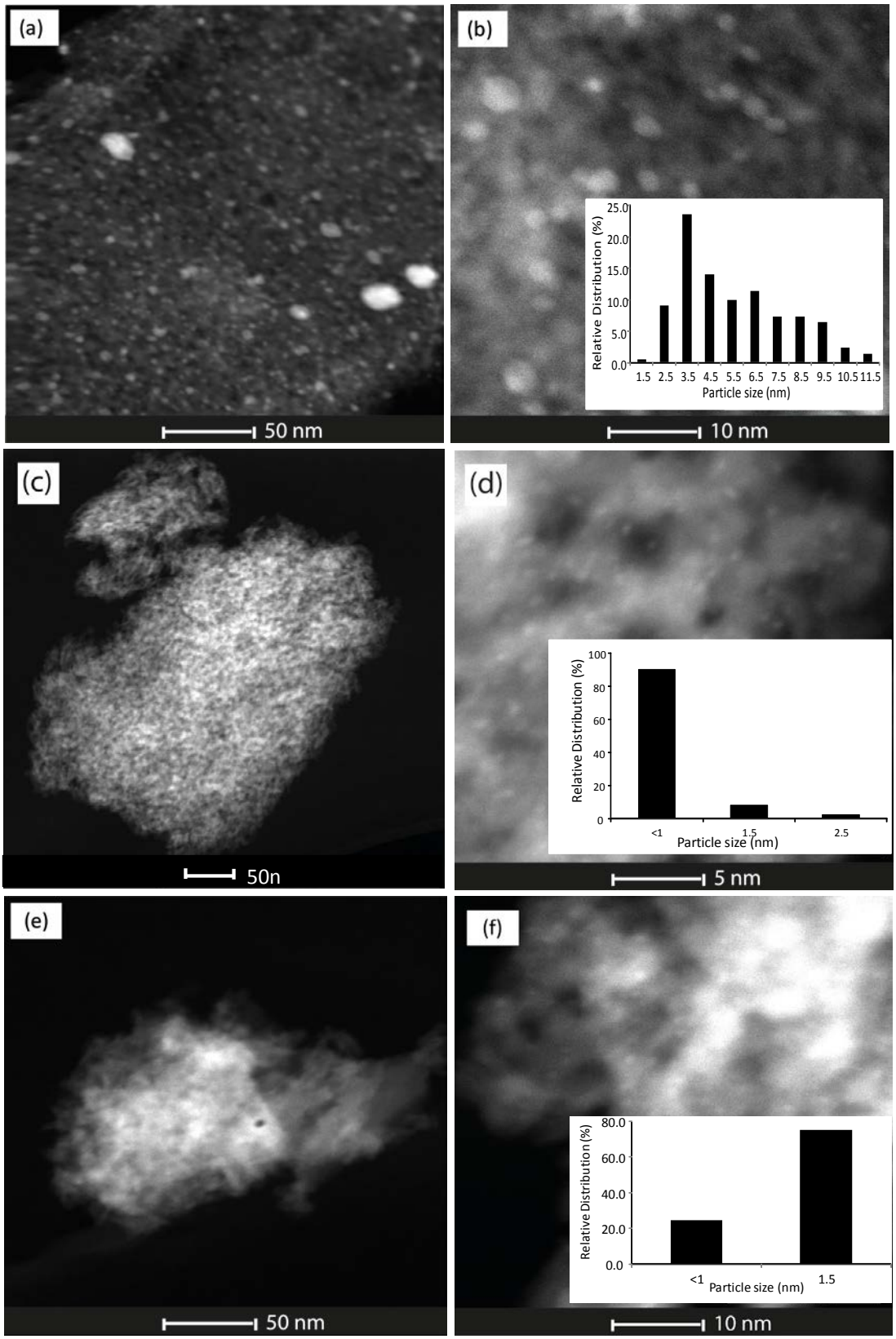

Fig. 1. Representative STEM images at two different magnifications and particle size distribution of catalysts used in reaction: (a,b) Ru(NN)/Al/M; (c,d) Ru(Cl)/Al/M y (e,f) Ru(acac)/Al/M.

3.2. Ru oxidation state characterization

Fig. 2 shows the deconvolution of XPS Ru signal according to the literature assignments [25-28]. In addition, the quantification of Ru/Al and $Ru^0/Ru_{(total)}$ atomic ratios determined by XPS are displayed in table 1. The Ru/Al ratio determined by XPS is similar for all the catalysts synthesized and these ratios are around twice that those determined by ICP. This result indicates that the surface of the alumina coating is enriched by Ru.

In the deconvolution of Ru 3d XPS signal of Ru(NN)/Al/M (spectrum a of Fig. 2) only the peaks at 279.1 eV and 280.5 eV are present, which are associated to Ru^0 and RuO_2 species [39–42], respectively. However, for the catalyst Ru(Cl)/Al/M and Ru(acac)/Al/M, besides the peaks associated to Ru^0 and RuO_2, is observed a new signal centered at 282.3 eV, which can be ascribed to hydrated RuO_2 species [43]. Additionally, a peak centered at 284.4 eV has been observed in all the catalysts which is attributed to carbon contamination.

The catalysts Ru(Cl)/Al/M and Ru(acac)/Al/M show $Ru^0/Ru_{(total)}$ ratios substantially smaller than the catalyst Ru(NN)Al/M. In the XPS spectra of Ru(Cl)/Al/M, a signal at 198.5 eV was observed indicating the presence of chlorine ions. It is well known that electronegative species such as chlorine can increase the oxidation state of metals [44,45], which could explain the lower $Ru^o/Ru_{(total)}$ ratios. However, the effect of electron-withdrawing species cannot be invoked to explain the lower $Ru^0/Ru_{(total)}$ ratios of Ru(acac)/Al/M. Therefore, the most plausible explanation is that metal oxidation state is governed by interaction with the support, which is particle-size dependent. Thus, the smaller the Ru particles, the stronger is the metal support interaction, leading to lower $Ru^0/Ru_{(total)}$ ratios.

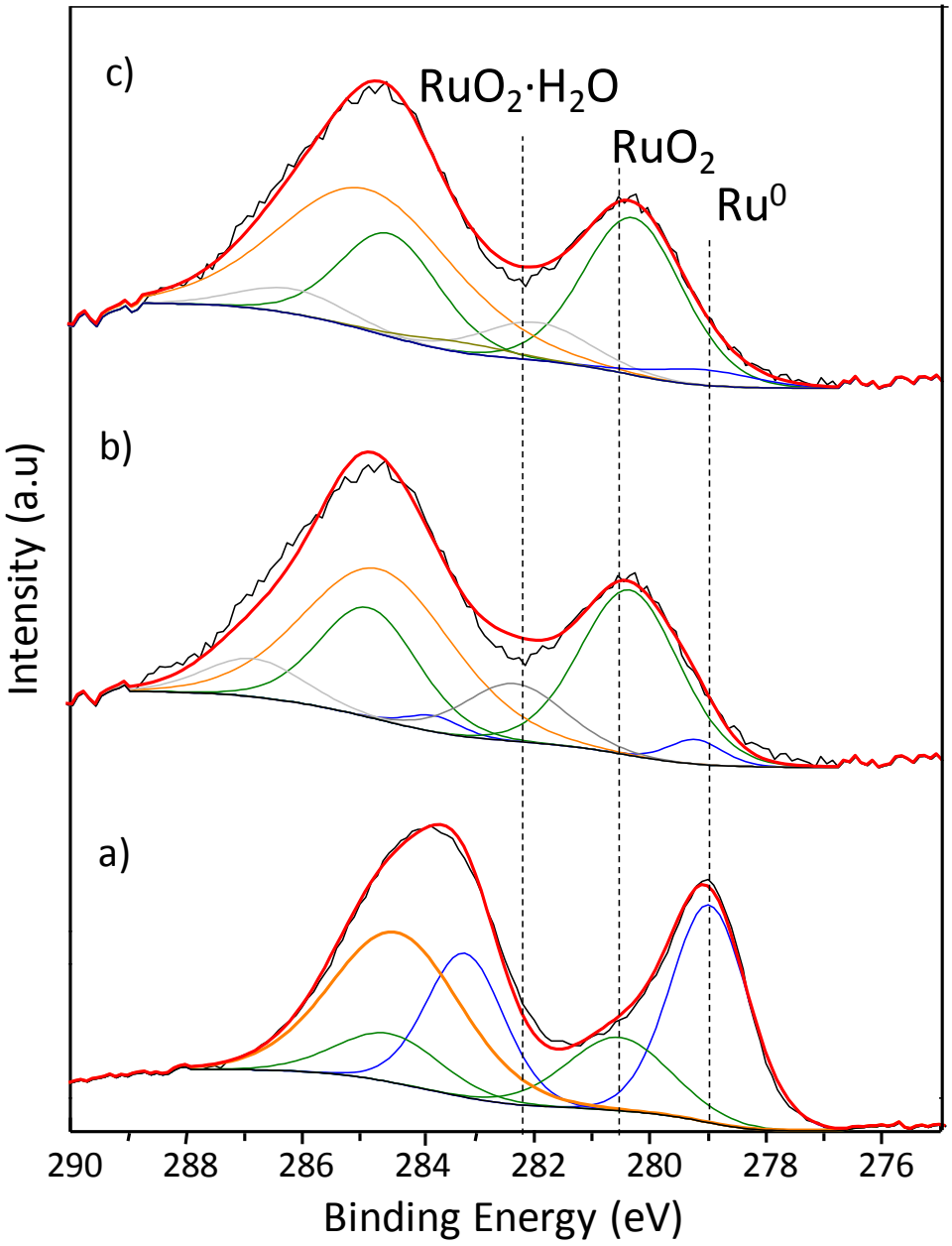

Fig. 2. XP Spectra of 3d core level of ruthenium of the catalyst used in reaction: (a) Ru(NN)/Al/M; (b) Ru(Cl)/Al/M and (c) Ru(acac)/Al/M.

The passivated catalysts after reaction were also studied by temperature programmed reduction (Fig. 3). The TPR profile of Ru(NN)/Al/M shows two peaks, one intense peak at low temperature (ca. 380 K) which can be attributed to surface oxidized large Ru nanoparticles and a broad peak at higher temperatures which can be attributed to oxidized smaller Ru particles, interacting strongly with the support. The other two catalysts, Ru(Cl)/Al/M and Ru(acac)/Al/M, exhibit similar TPR profiles with two

shoulders, one at ca.430 K and other in the range of 550-750 K which correspond to RuO_2 particles with some kind of interaction with support. The peak showed at low temperatures (380 K) is absent in these two latter catalysts, suggesting that the smaller particles, present in these catalysts, have stronger interaction with the support. On the other hand, the larger particles found for Ru(NN)/Al/M are oxidized only on the outermost surface but the inner bulk metal remains in reduced state in agreement with XPS results [21].

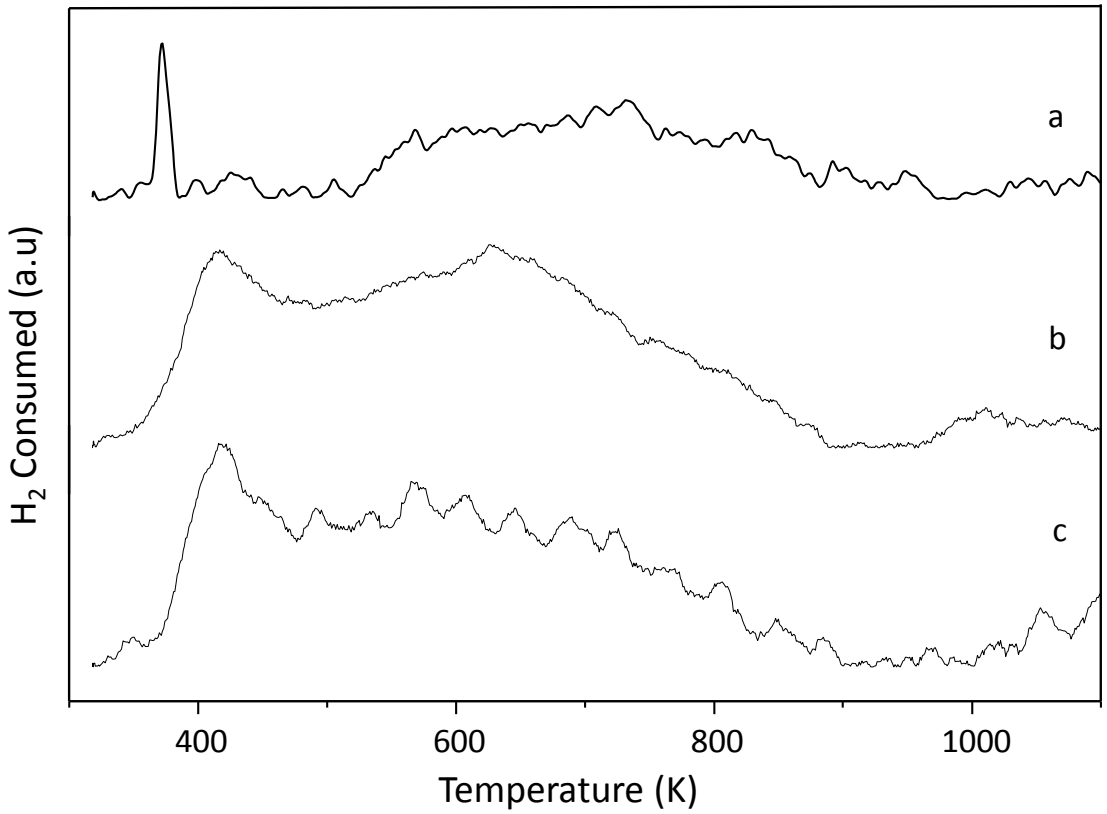

Fig. 3. TPR profile of catalysts passivated after reaction for Ru catalysts (a) Ru(NN)/Al/M; (b) Ru(Cl)/Al/M and (c) Ru(acac)/Al/M.

3.3. Catalytic testing in NH_3 decomposition

Fig. 4 shows the NH_3 conversion vs. temperature plot for the Ru-based catalysts. This figure also includes the curve obtained for the catalyst that contains a 15% Ni on Alumina coated monolith. The preparation and characterisation of this Ni/Al/M catalyst is reported in a previous publication [46]. All Ru-based catalyst exhibit higher

conversion than Ni-based catalyst although the metal loading is five-fold higher for the later, ca. 3 and 15wt.%/Al_2O_3, respectively. Noticeably, the mean particle size of Ni was larger than for Ru catalysts, 6 nm vs. 3.5 nm for Ru(NN)/Al/M. This seems to indicate a larger intrinsic activity of Ru metal, in agreement with the literature [21].

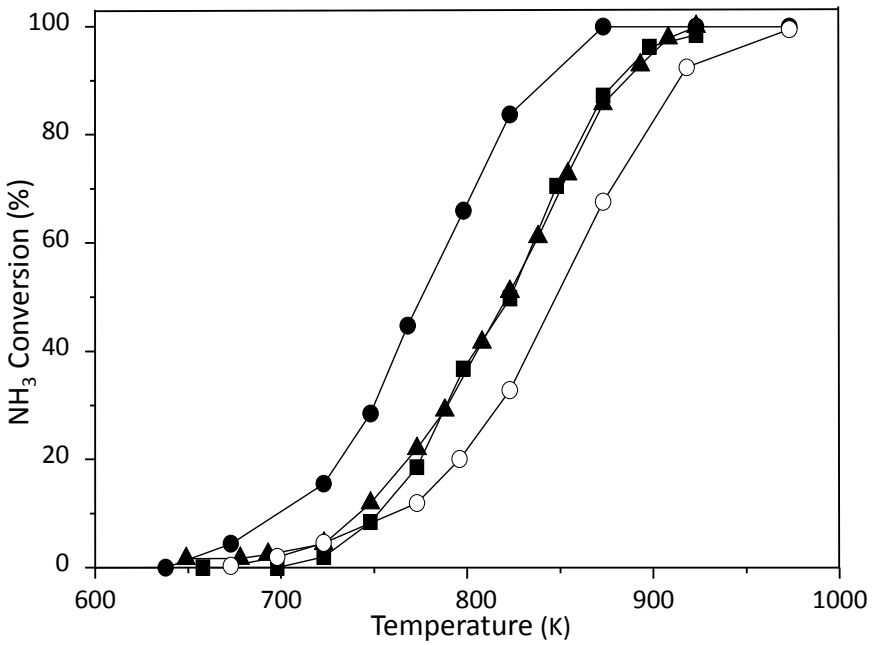

Fig. 4. NH_3 conversion at steady state as a function of the reaction temperature for different catalysts. (●) Ru(NN)/Al/M; (■) Ru(Cl)/Al/M; (▲) Ru(acac)/Al/M and (○) Ni/Al_2O_3/Monolith. Conditions:100 ml/min pure NH_3, space velocity: 35000 h^{-1}/g Ni/Al_2O_3.

Comparing among Ru-based catalysts, the one prepared with nitrosyl nitrate (Ru(NN)/Al/M) exhibits higher conversion, for all temperatures studied, than those prepared with other precursors. Since the main difference between Ru(NN)/Al/M and the other catalysts is the particle size, it is reasonable to think that this fact may be the responsible of the different catalytic behaviour. Jacobsen and coll. reported that B_5-type sites have the adequate geometry for the ammonia decomposition [47]. The number of these sites decreases as the particle size diminishes. This fact has been experimentally confirmed by several authors, who observed an increase of the turnover frequency as the metal particle size increased [48–50]. Xu and cols. [51] reported that there was an optimum Ru particle size of 2.2 nm that maximized turnover frequency. They also

found that the apparent activation energy increased from 79 kJ mol^{-1} to 122 kJ mol^{-1} as the mean Ru particle size decreased from 4.6 to 1.9 nm. The apparent activation energies of the different catalysts prepared were calculated from the Arrhenius equation (Fig. 5) at low conversion (<10%), in order to operate into differential condition. The apparent activation energy for Ru(NN)/Al/M was 104 kJ mol^{-1}, which was smaller than those determined for Ru(acac)/Al/M and Ru(Cl)/Al/M, 120 kJ mol^{-1} and 183 kJ mol^{-1}, respectively. It is possible that presence of chorine ions may act as inhibitor in the catalyst prepared with ruthenium chloride, contributing to the lower conversion and higher apparent activation energy for this catalyst.

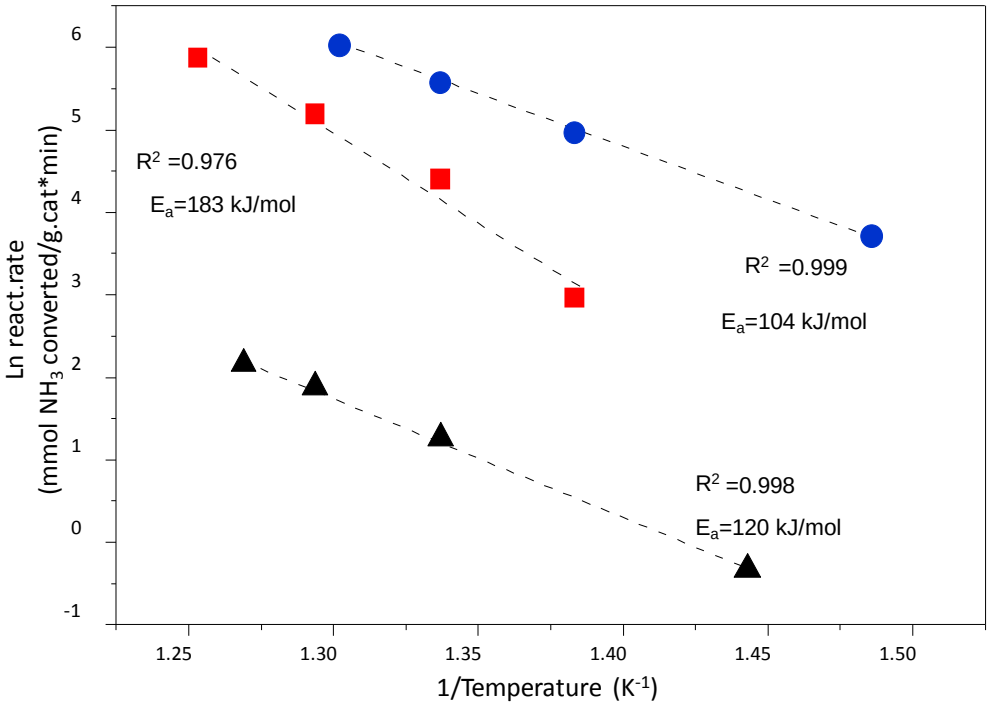

Fig. 5. Arrhenius plot and estimation of the apparent activation energies for the Ru catalysts from different precursors. (●) Ru(NN)/Al/M; (■) Ru(Cl)/Al/M; (▲) Ru(acac)/Al/M.

A long-term reaction was also evaluated to determine the stability of the Ru(NN)/Al/M catalyst (showing the best performance) after 15 h of reaction. The results show similar reaction profile for the same catalyst. However, a slight variation on the conversion was

299 measured (support information, Figure.S1). Considering the variation showed after long
300 reaction is around 5-7% less of measured during first run, it is possible to associate this
301 change to internal deviations of the analysis techniques and possible sintering effects.
302 However, thermal sintering of the metallic nanoparticles cannot be dismissed. This
303 phenomenon is strongly promoted by high operating temperatures. If the involved
304 mechanism is controlled by the diffusion of atoms trough the support, the sintering rate
305 correlates to Tamman temperature, but if the diffusion of atoms occurs at the outermost
306 surface, depends on the Hütting temperature [52]. Both parameters are closely related to
307 the melting point of metal catalyst (2607 K). In our case, the reaction temperature
308 reached 100 K degree above the Hütting temperature ($T_{Hütting}$ = 0.3 x $T_{melting}$ = 780 K),
309 which could be induce some sintering effects.
310
311 3.4. Mass and Heat Transfer Consideration
312 Monolithic reactors have attracted a huge interest to support catalytic material for many
313 applications in the last decades. Ones of the most important advantages are low
314 pressure-drop and large geometrical surface area compared to traditional packed bed
315 reactor. However, taking into account that reactant must diffuse from gas-solid phase,
316 and flow developed inside the monolithic channel present characteristic, mass and heat
317 transfer limitation have been considered for many authors has an interesting topic to
318 analyses and avoid the reaction will be controlled by diffusion phenomena.
319 In this work, the possible problems of mass transfer were evaluated by performing
320 previous experiments at different linear velocities of the feed gas, keeping the spatial
321 velocity constant, in the operating range used (spatial time $1.827x10^{-5}$ mol/g.min), any
322 significant differences in the conversion were observed when increasing the linear
323 velocity of the gas.

Otherwise, the restrictions due to internal diffusion were evaluated by the Weisz-Prater criterion [53], assuming a particle size equivalent to 1/3 of the thickness of the layer of product deposited in the monolith (the thickness of alumina coating deposited and measured by EDX-SEM Mapping was 2.7μm). In the conditions of operation studied in this work, this criterion takes values lower than 0.1, indicating that the effects of internal diffusion are not important.

Regarding the influence of the thermal effects, and the moderately endothermic character (86 kJ/mol) of the reaction, in the operating conditions where the restrictions of matter transfer are minimized, the calculation of the Anderson criterion and of Mears [54,55], assuming as effective particle radius 1/3 of the thickness of the catalytic layer, also confirming that the effects of heat transmission are negligible in the evaluation of the catalytic activity and the kinetic parameters observed.

Given that the flow developed inside monolith channel is of laminar-type, the reacting species must be transferred to from the gas stream to the monolith wall by molecular diffusion. This fact linked to large values of the reaction rate may cause that mass transfer phenomena will be the reaction controlling step. However, combining a proper synthesis process, and tuning the specific reaction conditions it can be improved the surface contact. Another way to enhance the contact surface area between gas and solid phases is to induce turbulences inside the monolith channels, or to enhance axial diffusion between them.

Additionally, other way to reach higher performance of these type of reactors is achieving a closer interaction between gas-solid phase by modifying the rugosity of the walls. Carbon nanofibers can form aggregates with high surface area, high mesopore volumes and low tortuosity. Additionally, the possibility to manipulate diameter and length as well as the bulk density of CNF, open an opportunity to tailor the porosity and

overcome tortuosity problems. This reduces or eliminates the internal diffusion limitations by preventing concentration gradients inside the monolith channels. This situation is very favorable for fast and highly exothermic gas-phase reactions, and for sluggish liquid phase reactions because mass/heat transfer limitations are prevented while keeping low pressure drop. In fact, the advantages of incorporating this kind of materials has been investigated by our groups previously. The effect to anchor carbon nanofibers (CNF) and N-doped carbon nanofibers (N-CNF) to the alumina washcoated monolith for ammonia decomposition and other reactions have shown results very promising [15,56]. Modify the surface channels by carbon or other nanomaterials open a new possibility to take advantages of structured reactors and at the same time reduce mass and heat transfer phenomena.

3.5. Kinetic Model

The development of an efficient reactor requires necessarily a depth understanding of kinetic aspects. Many researches related to ammonia decomposition reaction have been carried out under high vacuum condition and with model catalysts. These conditions are not comparable to fuel cell systems fed by ammonia decomposition reaction where usually high ammonia concentration, atmospheric pressure and high temperature have.

Regarding to ammonia decomposition kinetics, many authors have fitted the experimental data using the Themkyn-Pyzhev model:

$$(-rNH_3) = k\left[\left(\frac{{PNH_3}^2}{{PH_2}^3}\right)^m - \frac{{PN_2}^2}{Keq^2}\left(\frac{{PH_2}^3}{{PNH_3}^2}\right)\right] \quad (1)$$

Where m is a constant related to the non-uniformity surface, and the second term corresponds to the contribution of the reversible equation (i.e. que driving force to the equilibrium). According with the experimental conditions (673 K -1023 K), and to the

results previously reported [57], this term is virtually zero, indicating that the reaction is not limited by equilibrium, and therefore this contribution can be neglected.

The Temkin-Pyzhev model may be rewrite to the power law rate expression:

$$(-rNH_3) = k' P\mathrm{NH_3}^{\alpha} P\mathrm{H_2}^{\beta} \quad (2)$$

where k and k` follows an Arrhenius dependence with the temperature, [32,58,59] and α and β are the kinetic orders with respect ammonia and hydrogen, respectively.

The kinetic parameters were calculated by non-linear multivariable regression using Levenberg–Marquardt algorithm coupled to a Runge–Kutta–Fehlberg routine, using the steady-state ammonia mass balance in plug-flow reactor, [57]:

$$(-r_{NH3}) = \frac{dX_{NH_3}}{d(W_{cat}/F^0_{NH_3})} \quad (3)$$

X_{NH_3} is the ammonia conversion, W_{cat} / F^0_{NH3} is the spatial time (g_{cat} s/mol NH_3) and $(-r_{NH_3})$ is given by the power-law rate expression (2). The numerical solution of eqn (3), allows the calculation of the sum of the squared residuals (SSR), used as objective function minimized by the Levenberg–Marquardt algorithm:

$$SSR = \min \sum_{i=1}^{i=n} \left(X^{exp}_{NH_3} - X^{calc}_{NH_3}\right)^2 \quad (4)$$

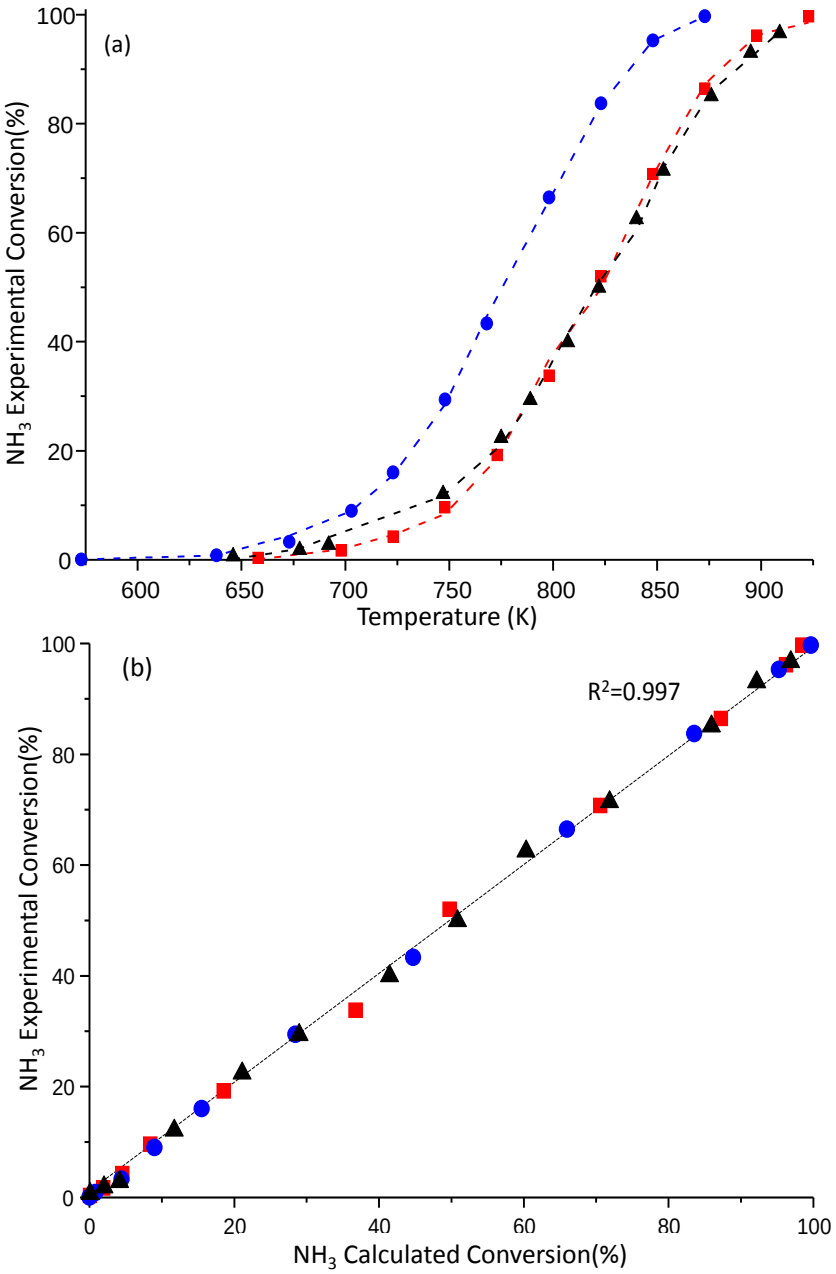

Fig. 6. (a) Dependence of NH3 conversion with reaction temperature (symbols: experimental data; dotted line: model simulation, eqn. 2). (●) Ru(NN)/Al/M; (■) Ru(Cl)/Al/M; (▲) Ru(acac)/Al/M; (b) Parity plot of the NH3 conversion data.

Fig.6 a-b, shows the results of the experimental and model prediction of ammonia conversion vs. temperature data; and their excellent correlation in the parity plot (Fig. 6, b). As is in these figures the homoscedastic distribution of the errors along the entire range of conversions, indicates that power law model is an excellent approximation for the modelling of the experimental data and, according to the main hypothesis of the

Temkin-Pyzhev model, the rate determining step of the reaction mechanism is the associative adsorption of N-adsorbed species.

In the Table 2 are shown the kinetic parameters of the Temkin-Pyzhev model. The low values of the standard errors obtained in all the cases, indicate again the excellent fitting achieved, and therefore the validity of the model. Thus, the valued of the apparent activation energies presented in the Table 2 have the same tendency (i.e. Ru(NN)/Al/M < Ru(Cl)/Al/M < Ru(acac)/Al/M) that the one obtaiend by direct aplication of the Arrhenius equation to the low conversion data (Fig. 5). The good coincidence between the results obtaiend using the diferential method of the low conversion data (Figure 5) and the integral method of whole range of conversion data, eqn. 3 and Figure 6, if an aditional proof of the confidence of the aproach used here.

Table 2: Kinetic parameters of Temkin-Pyzhev model.

Catalyst	$Ru(NN)/Al_2O_3/M$	$Ru(acac)/Al_2O_3/M$	$Ru(Cl)/Al_2O_3/M$
Parameter	Value	Value	Value
k (*)	$6.99\ x10^{-04}$±$4.22\ x10^{-5}$	$1.94\ x10^{-04}$±$1.89\ x10^{-5}$	$1.04\ x10^{-02}$± $4.29\ x10^{-7}$
Ea(kJ/mol)	76.63±6.22	154.81±12.50	89.32±4.80
α	0.72±0.05	1.046±0.10	0.781±0.06
β	0.45±0.01	-0.278±0.02	0.439±0.03
$-(\alpha/\beta)$	-1.57±0.06	3.75±0.12	-1.78±0.09

* units: mol $NH_3 \cdot atm^{(\alpha+\beta)}/g_{cat} \cdot s$

According to the "Temkin formalism", the ratio α/β should be between 0.4 and 0.5, however the result calculated by the fiting of the data on Figure 2 shows large differences. In fact, the kinetic orders of ammonia and hydorgen show a great varibility each other, which could be associated to the different catalyst intrinsinc nature, mainly the average and distribution of particle sizez, the Ru content, and even the shape of the particles, [33,60,61].

The lower activation energy and higher conversion of catalyst Ru(NN)/Al/M, compared to those prepared from the other precursors, can be attributed to its larger mean particle size (3.5 nm) which entails higher density of B_5-type sites. This behavior has been

419 explained by compensatory effects [51,62], derived from the relationship between the
420 activation energy of the rate-limiting step, and the stability of the reaction intermediates
421 on the surface of the catalyst.
422 In spite of that the Temkin-Pyzhev model provide an reasonable acknowledge of the
423 kinetic reaction mechanism, and a simple way to analyze the data, in some cases it is
424 necesary to use a more robust model, which can predict the kinetic order evolutions
425 during ammonia decomposition reaction. The kinetic orders and the apparent energies
426 of activation shown in Table 2 are an average of all the individual values which could
427 be calculated as the gas composition changes along the reactor length. In fact, we have
428 previously demonstrated [57], that the variable kinetic orders and apparent activation
429 energies frequently reported in the literature are consequence of misleading data
430 analysis, and not a consequence of the any change in the controlling step of the reaction
431 mechanism.
432
433 **4. Conclusions**
434 The results of this work show that the Ru catalyst in the form of honeycomb monoliths
435 is a robust an active catalyst for H_2 generation form ammonia decomposition, thus
436 being an enabling technology for the use of ammonia as practical H_2 storage media.
437 All the Ru-based catalysts used exhibited higher conversion in the decomposition of
438 pure ammonia than Ni-based one, despite of ca. 5-fold larger metal loading of the latter.
439 Among all the Ru-based catalysts, the highest conversion and lowest apparent activation
440 energy correspond to that prepared using ruthenium-nitrosyl-nitrate as precursor. This
441 catalyst exhibited the largest mean particle size and the highest ratio of $Ru^0/Ru_{(total)}$ in
442 reduced state after the passivation step. Thus, the highest activity of Ru prepared from

443 nitrosyl-nitrate could be explained by the higher proportion of B_5-type sites exposed,
444 which have been related to particles with the same order of size.
445 The Temkin-Pyzhev (Power-Law) kinetic model provide an reasonable acknowledge of
446 the reaction mechanism, and a simple way to analyze the data, in the whole range of
447 ammonai conversions. The values of the kinetic orders, and the apparent energies of
448 activation shown in Table 2, are valid to discriminate the intrisic differences observed
449 between the catalysts, and to develop a complete model of the monolithic reactor.
450

451 **Aknowledgements**

452 The authors wants to aknowledge to the support of European Commission (FP7, Grant
453 agreement nº 280658). Dr Armenise wants to aknowledge specially to University of
454 Zaragoza, Institute of Carboquimica and Banco Santander Hispano to finance the
455 doctoral fellow. Finnaly the authors wants to aknowledge to Universida Politecnica
456 Salesiana to provide the economical support to attend the IMCCRE-2018.
457
458

References

[1] Mori D, Hirose K. Recent challenges of hydrogen storage technologies for fuel cell vehicles. International Journal of Hydrogen Energy 2009;34:4569–74. doi:http://dx.doi.org/10.1016/j.ijhydene.2008.07.115.

[2] Sakintuna B, Lamari-Darkrim F, Hirscher M. Metal hydride materials for solid hydrogen storage: A review. International Journal of Hydrogen Energy 2007;32:1121–40. doi:http://dx.doi.org/10.1016/j.ijhydene.2006.11.022.

[3] Schlapbach L, Zuttel A. Hydrogen-storage materials for mobile applications. Nature 2001;414:353–8.

[4] Holladay JD, Hu J, King DL, Wang Y. An overview of hydrogen production technologies. Catalysis Today 2009;139:244–60. doi:http://dx.doi.org/10.1016/j.cattod.2008.08.039.

[5] Cheng X, Shi Z, Glass N, Zhang L, Zhang J, Song D, et al. A review of PEM hydrogen fuel cell contamination: Impacts, mechanisms, and mitigation. Journal of Power Sources 2007;165:739–56. doi:http://dx.doi.org/10.1016/j.jpowsour.2006.12.012.

[6] Dasireddy VDBC, Likozar B. COx-free hydrogen generation via decomposition of ammonia over copper and zinc-based catalysts. Fuel 2017;196:325–35. doi:https://doi.org/10.1016/j.fuel.2017.01.117.

[7] Schuth F, Palkovits R, Schlogl R, Su DS. Ammonia as a possible element in an energy infrastructure: catalysts for ammonia decomposition. Energy Environ Sci 2012;5:6278–89. doi:10.1039/C2EE02865D.

[8] Yin SF, Xu BQ, Zhou XP, Au CT. A mini-review on ammonia decomposition catalysts for on-site generation of hydrogen for fuel cell applications. Applied Catalysis A: General 2004;277:1–9. doi:http://dx.doi.org/10.1016/j.apcata.2004.09.020.

[9] Ganley JC, Seebauer EG, Masel RI. Development of a microreactor for the production of hydrogen from ammonia. Journal of Power Sources 2004;137:53–61. doi:http://dx.doi.org/10.1016/j.jpowsour.2004.05.032.

[10] Bradford MCJ, Fanning PE, Vannice MA. Kinetics of NH3Decomposition over Well Dispersed Ru. Journal of Catalysis 1997;172:479–84. doi:http://dx.doi.org/10.1006/jcat.1997.1877.

[11] Pyrz W, Vijay R, Binz J, Lauterbach J, Buttrey DJ. Characterization of K-Promoted Ru Catalysts for Ammonia Decomposition Discovered Using High-Throughput Experimentation. Topics in Catalysis 2008;50:180–91. doi:10.1007/s11244-008-9095-y.

[12] Ju X, Liu L, Yu P, Guo J, Zhang X, He T, et al. Mesoporous Ru/MgO prepared by a deposition-precipitation method as highly active catalyst for producing COx-free hydrogen from ammonia decomposition. Applied Catalysis B: Environmental 2017;211:167–75. doi:https://doi.org/10.1016/j.apcatb.2017.04.043.

[13] Raróg-Pilecka W, Szmigiel D, Kowalczyk Z, Jodzis S, Zielinski J. Ammonia decomposition over the carbon-based ruthenium catalyst promoted with barium or cesium. Journal of Catalysis 2003;218:465–9. doi:http://dx.doi.org/10.1016/S0021-9517(03)00058-7.

[14] Sørensen RZ, Klerke A, Quaade U, Jensen S, Hansen O, Christensen CH. Promoted Ru on high-surface area graphite for efficient miniaturized production of hydrogen from ammonia. Catalysis Letters 2006;112:77–81. doi:10.1007/s10562-006-0167-y.

[15] Armenise S, Roldán L, Marco Y, Monzón A, García-Bordejé E. Elucidation of Catalyst Support Effect for NH3 Decomposition Using Ru Nanoparticles on Nitrogen-Functionalized Carbon Nanofiber Monoliths. The Journal of Physical Chemistry C 2012;116:26385–95. doi:10.1021/jp308985x.
[16] Chen J, Zhu ZH, Wang S, Ma Q, Rudolph V, Lu GQ. Effects of nitrogen doping on the structure of carbon nanotubes (CNTs) and activity of Ru/CNTs in ammonia decomposition. Chemical Engineering Journal 2010;156:404–10. doi:http://dx.doi.org/10.1016/j.cej.2009.10.062.
[17] García-García FR, Álvarez-Rodríguez J, Rodríguez-Ramos I, Guerrero-Ruiz A. The use of carbon nanotubes with and without nitrogen doping as support for ruthenium catalysts in the ammonia decomposition reaction. Carbon 2010;48:267–76. doi:http://dx.doi.org/10.1016/j.carbon.2009.09.015.
[18] Zheng W, Zhang J, Zhu B, Blume R, Zhang Y, Schlichte K, et al. Structure–Function Correlations for Ru/CNT in the Catalytic Decomposition of Ammonia. ChemSusChem 2010;3:226–30. doi:10.1002/cssc.200900217.
[19] Duan X, Qian G, Zhou X, Chen D, Yuan W. MCM-41 supported CoMo bimetallic catalysts for enhanced hydrogen production by ammonia decomposition. Chemical Engineering Journal 2012;207:103–8. doi:http://dx.doi.org/10.1016/j.cej.2012.05.100.
[20] Jacobsen CJH, Dahl S, Clausen BS, Bahn S, Logadottir A, Nørskov JK. Catalyst Design by Interpolation in the Periodic Table: Bimetallic Ammonia Synthesis Catalysts. Journal of the American Chemical Society 2001;123:8404–5. doi:10.1021/ja010963d.
[21] Boisen A, Dahl S, Nørskov JK, Christensen CH. Why the optimal ammonia synthesis catalyst is not the optimal ammonia decomposition catalyst. Journal of Catalysis 2005;230:309–12. doi:http://dx.doi.org/10.1016/j.jcat.2004.12.013.
[22] Czekajło Ł, Lendzion-Bieluń Z. Effect of preparation conditions and promoters on the structure and activity of the ammonia decomposition reaction catalyst based on nanocrystalline cobalt. Chemical Engineering Journal 2016;289:254–60. doi:http://dx.doi.org/10.1016/j.cej.2015.12.093.
[23] Srifa A, Okura K, Okanishi T, Muroyama H, Matsui T, Eguchi K. Hydrogen production by ammonia decomposition over Cs-modified Co3Mo3N catalysts. Applied Catalysis B: Environmental 2017;218:1–8. doi:https://doi.org/10.1016/j.apcatb.2017.06.034.
[24] Christian, Mitchell M, Kim D-P, Kenis PJA. Ceramic microreactors for on-site hydrogen production. Journal of Catalysis 2006;241:235–42. doi:http://dx.doi.org/10.1016/j.jcat.2006.04.033.
[25] Deshmukh SR, Mhadeshwar AB, Vlachos DG. Microreactor Modeling for Hydrogen Production from Ammonia Decomposition on Ruthenium. Industrial & Engineering Chemistry Research 2004;43:2986–99. doi:10.1021/ie030557y.
[26] Ganley JC, Thomas FS, Seebauer EG, Masel RI. A Priori Catalytic Activity Correlations: The Difficult Case of Hydrogen Production from Ammonia. Catalysis Letters 2004;96:117–22. doi:10.1023/B:CATL.0000030108.50691.d4.
[27] Plana C, Armenise S, Monzón A, García-Bordejé E. Ni on alumina-coated cordierite monoliths for in situ generation of CO-free H2 from ammonia. Journal of Catalysis 2010;275:228–35. doi:http://dx.doi.org/10.1016/j.jcat.2010.07.026.
[28] Löffler DG, Schmidt LD. Kinetics of NH3 decomposition on polycrystalline Pt. Journal of Catalysis 1976;41:440–54. doi:http://dx.doi.org/10.1016/0021-9517(76)90245-1.
[29] Vajo JJ, Tsai W, Weinberg WH. Steady-state decomposition of ammonia on the

platinum(110)-(1 .times. 2) surface. The Journal of Physical Chemistry 1986;90:6531–5. doi:10.1021/j100282a023.
[30] Tsai W, Weinberg WH. Steady-state decomposition of ammonia on the ruthenium(001) surface. The Journal of Physical Chemistry 1987;91:5302–7. doi:10.1021/j100304a034.
[31] Kunsman CH. THE THERMAL DECOMPOSITION OF AMMONIA ON IRON CATALYSTS. II. Journal of the American Chemical Society 1929;51:688–95. doi:10.1021/ja01378a005.
[32] Tamaru K. A “new” general mechanism of ammonia synthesis and decomposition on transition metals. Accounts of Chemical Research 1988;21:88–94. doi:10.1021/ar00146a007.
[33] Chellappa AS, Fischer CM, Thomson WJ. Ammonia decomposition kinetics over Ni-Pt/Al2O3 for PEM fuel cell applications. Applied Catalysis A: General 2002;227:231–40. doi:http://dx.doi.org/10.1016/S0926-860X(01)00941-3.
[34] Nishida T, Egawa C, Naito S, Tamaru K. Hydrogenation of nitric oxide on (0 0 1) and (1 1 10) surfaces of ruthenium. J Chem Soc{,} Faraday Trans 1 1984;80:1567–78. doi:10.1039/F19848001567.
[35] Djéga-Mariadassou G, Shin C-H, Bugli G. Tamaru’s model for ammonia decomposition over titanium oxynitride. Journal of Molecular Catalysis A: Chemical 1999;141:263–7. doi:http://dx.doi.org/10.1016/S1381-1169(98)00270-2.
[36] D’Souza L, Regalbuto JR, Miller JT. Preparation of carbon supported cobalt by electrostatic adsorption of [Co(NH3)6]Cl3. Journal of Catalysis 2008;254:157–69. doi:http://dx.doi.org/10.1016/j.jcat.2007.12.007.
[37] Nijhuis TA, Beers AEW, Vergunst T, Hoek I, Kapteijn F, Moulijn JA. Preparation of monolithic catalysts. Catalysis Reviews 2001;43:345–80. doi:10.1081/CR-120001807.
[38] García-Bordejé E, Kvande I, Chen D, Rønning M. Synthesis of composite materials of carbon nanofibres and ceramic monoliths with uniform and tuneable nanofibre layer thickness. Carbon 2007;45:1828–38. doi:http://dx.doi.org/10.1016/j.carbon.2007.04.026.
[39] Chan HYH, Takoudis CG, Weaver MJ. High-Pressure Oxidation of Ruthenium as Probed by Surface-Enhanced Raman and X-Ray Photoelectron Spectroscopies. Journal of Catalysis 1997;172:336–45. doi:http://dx.doi.org/10.1006/jcat.1997.1841.
[40] Elmasides C, Kondarides DI, Grünert W, Verykios XE. XPS and FTIR Study of Ru/Al2O3 and Ru/TiO2 Catalysts: Reduction Characteristics and Interaction with a Methane−Oxygen Mixture. The Journal of Physical Chemistry B 1999;103:5227–39. doi:10.1021/jp9842291.
[41] Mazzieri V, Coloma-Pascual F, Arcoya A, L’Argentière PC, Fı́goli NS. XPS, FTIR and TPR characterization of Ru/Al2O3 catalysts. Applied Surface Science 2003;210:222–30. doi:http://dx.doi.org/10.1016/S0169-4332(03)00146-6.
[42] Okal J, Zawadzki M, Tylus W. Microstructure characterization and propane oxidation over supported Ru nanoparticles synthesized by the microwave-polyol method. Applied Catalysis B: Environmental 2011;101:548–59. doi:http://dx.doi.org/10.1016/j.apcatb.2010.10.028.
[43] Rolison DR, Hagans PL, Swider KE, Long JW. Role of Hydrous Ruthenium Oxide in Pt−Ru Direct Methanol Fuel Cell Anode Electrocatalysts: The Importance of Mixed Electron/Proton Conductivity. Langmuir 1999;15:774–9.

doi:10.1021/la9807863.
[44] Zhong Z, Aika K. Effect of ruthenium precursor on hydrogen-treated active carbon supported ruthenium catalysts for ammonia synthesis. Inorganica Chimica Acta 1998;280:183–8. doi:http://dx.doi.org/10.1016/S0020-1693(98)00202-3.
[45] Maroto-Valiente A, Cerro-Alarcón M, Guerrero-Ruiz A, Rodríguez-Ramos I. Effect of the metal precursor on the surface site distribution of Al2O3-supported Ru catalysts: catalytic effects on the n-butane/H2 test. Applied Catalysis A: General 2005;283:23–32. doi:http://dx.doi.org/10.1016/j.apcata.2004.12.047.
[46] Plana C, Armenise S, Monzón A, García-Bordejé E. Ni on alumina-coated cordierite monoliths for in situ generation of CO-free H2 from ammonia. Journal of Catalysis 2010;275. doi:10.1016/j.jcat.2010.07.026.
[47] Jacobsen CJH, Dahl S, Hansen PL, Törnqvist E, Jensen L, Topsøe H, et al. Structure sensitivity of supported ruthenium catalysts for ammonia synthesis. Journal of Molecular Catalysis A: Chemical 2000;163:19–26. doi:http://dx.doi.org/10.1016/S1381-1169(00)00396-4.
[48] Choudhary T V, Sivadinarayana C, Goodman DW. Catalytic ammonia decomposition: COx-free hydrogen production for fuel cell applications. Catalysis Letters 2001;72:197–201. doi:10.1023/A:1009023825549.
[49] García-García FR, Guerrero-Ruiz A, Rodríguez-Ramos I. Role of B5-Type Sites in Ru Catalysts used for the NH3 Decomposition Reaction. Topics in Catalysis 2009;52:758–64. doi:10.1007/s11244-009-9203-7.
[50] Karim AM, Prasad V, Mpourmpakis G, Lonergan WW, Frenkel AI, Chen JG, et al. Correlating Particle Size and Shape of Supported Ru/γ-Al2O3 Catalysts with NH3 Decomposition Activity. Journal of the American Chemical Society 2009;131:12230–9. doi:10.1021/ja902587k.
[51] Zheng W, Zhang J, Xu H, Li W. NH3 Decomposition Kinetics on Supported Ru Clusters: Morphology and Particle Size Effect. Catalysis Letters 2007;119:311–8. doi:10.1007/s10562-007-9237-z.
[52] Liu H. AMMONIA SYNTHESIS CATALYSTS: Innovation and Practice. Cao Xiangh. Beijing: World Scientific Publishing Co. Pte. Ltd; 2013.
[53] Weisz PB, Prater CD. Interpretation of Measurements in Experimental Catalysis. In: Frankenburg WG, Komarewsky VI, Rideal EK, editors. vol. 6, Academic Press; 1954, p. 143–96. doi:https://doi.org/10.1016/S0360-0564(08)60390-9.
[54] Holmgren A, Andersson B. Mass transfer in monolith catalysts–CO oxidation experiments and simulations. Chemical Engineering Science 1998;53:2285–98. doi:https://doi.org/10.1016/S0009-2509(98)00080-3.
[55] Mears DE. Diagnostic criteria for heat transport limitations in fixed bed reactors. Journal of Catalysis 1971;20:127–31. doi:https://doi.org/10.1016/0021-9517(71)90073-X.
[56] Restivo J, Órfão JJM, Pereira MFR, Vanhaecke E, Rönning M, Iouranova T, et al. Catalytic ozonation of oxalic acid using carbon nanofibres on macrostructured supports. Water Science and Technology 2012;65. doi:10.2166/wst.2012.882.
[57] Armenise S, García-Bordejé E, Valverde JL, Romeo E, Monzón A. A Langmuir-Hinshelwood approach to the kinetic modelling of catalytic ammonia decomposition in an integral reactor. Physical Chemistry Chemical Physics 2013;15. doi:10.1039/c3cp50715g.
[58] Emmett PH, Kummer JT. Kinetics of Ammonia Synthesis. Industrial & Engineering Chemistry 1943;35:677–83. doi:10.1021/ie50402a012.
[59] M. Temkin VP. Kinetics of the synthesis of ammonia on promoted iron catalysts. Acta Physicochim URSS, 1939;12:327–56.

[60] Bell TE, Torrente-Murciano L. H2 Production via Ammonia Decomposition Using Non-Noble Metal Catalysts: A Review. Topics in Catalysis 2016;59:1438–57. doi:10.1007/s11244-016-0653-4.
[61] Zhang J, Xu H, Li W. Kinetic study of NH3 decomposition over Ni nanoparticles: The role of La promoter, structure sensitivity and compensation effect. Applied Catalysis A: General 2005;296:257–67. doi:https://doi.org/10.1016/j.apcata.2005.08.046.
[62] Bligaard T, Honkala K, Logadottir A, Nørskov JK, Dahl S, Jacobsen CJH. On the Compensation Effect in Heterogeneous Catalysis. The Journal of Physical Chemistry B 2003;107:9325–31. doi:10.1021/jp034447g.